

# Defects and impurities in graphene-like materials

Graphene-like materials could be used in the fabrication of electronic and optoelectronic devices, gas sensors, biosensors, and batteries for energy storage. Since it is almost impossible to work with defect-free or impurity-free materials, it is essential to understand how defects and impurities alter the electronic and vibrational properties of these systems. Technologically speaking it is more important to distinguish between different types of defects (impurities) and determine if their presence is desirable or not. This review discusses these issues and provides an updated overview of the current characterization tools able to identify and detect defects in different forms of graphene.

Paulo T. Araujo<sup>a</sup>, Mauricio Terrones<sup>b,c</sup>, and Mildred S. Dresselhaus<sup>a,d,\*</sup>

<sup>a</sup>Department of Electrical Engineering and Computer Sciences, Massachusetts Institute of Technology, Cambridge, MA 02139, USA

<sup>b</sup>Department of Physics, Department of Materials Science and Engineering and Materials Research Institute, The Pennsylvania State University, University Park, PA 16802, USA

<sup>c</sup>Research Center for Exotic Nanocarbons (JST), Shinshu University, Wakasato 4-17-1, Nagano-city 380-8553, Japan

<sup>d</sup>Department of Physics, Massachusetts Institute of Technology, Cambridge, MA 02139, USA

\*E-mail: [millie@mgm.mit.edu](mailto:millie@mgm.mit.edu)

Defects in materials are normally considered to be detrimental to the properties of materials and to devices based on such materials. However, defects can also be beneficial to materials in providing dopants to control both their carrier concentration and whether the carriers are *n*-type or *p*-type<sup>1-16</sup>. Isotopic defects can also be used to probe materials' properties by separating their electronic properties from behaviors associated with their phonon dynamics. Isotopic defects consist of defects that do not alter the electronic properties of the material. Because of the significant percentage difference between the mass of the <sup>12</sup>C and <sup>13</sup>C isotopic species, the graphene phonon frequencies for <sup>13</sup>C isotopes differ sufficiently from those of <sup>12</sup>C so that they can be used to probe related phonon

phenomena in a layered compound such as graphene, without changing the electronic properties<sup>17-25</sup>.

In this review we also consider defect-induced modifications to few-layer graphene, one of the simplest systems under current investigation in materials science, and yet informative about the effects of defects and their relevance to the functional performance of materials<sup>26-31</sup>. In this context we consider in-plane defects, which occur ubiquitously in few-layer graphene, whether we are considering a single layer or a thin film of ten layers. In-plane defects are symmetry-breaking and can include point defects, such as vacancies<sup>32-47</sup>, substitutional impurities<sup>1-16</sup>, or interstitial impurities<sup>1-16</sup>, and the impurity can be a chemical impurity or an isotopic impurity<sup>17-25</sup>. Grain-boundary defects have been observed

in graphene prepared by chemical vapor deposition (CVD) but they also occur in mechanically exfoliated graphene, though some differences in properties are found when comparing these two types of graphene<sup>48-51</sup>. Sample boundaries or edges are also symmetry-breaking defects, but are interesting in their own right, especially for the case of narrow ribbons where electron and phonon mean free paths are longer than the ribbon widths, so that these boundaries serve as scattering centers for electrons and phonons<sup>1,2,52-58</sup>. Also of interest are interplanar defects, such as stacking faults within interlayer stackings, different interplanar isotopic arrangements, or different chemical arrangements that might be synthesized for the study of specific graphene-related phenomena<sup>39</sup>. In order to understand the effects of the various interesting defects, in graphene-like systems that occur or are intentionally introduced, a variety of experimental probes are used, and in this review special emphasis will be given to atomic-level structural information derived from aberration corrected high-resolution transmission electron microscopy<sup>1,35,36,59-63</sup>, scanning tunneling microscopy<sup>1,64-66</sup>, and spectroscopic information derived from Raman<sup>1,2,58,67-71</sup> and scanning tunneling spectroscopies<sup>1,64-66</sup>.

## Types of defect

In this review we consider structural defects associated with both naturally occurring imperfections and growth-induced defects<sup>1-25</sup>, on one hand, and defects introduced for enhancing the understanding of graphene-related phenomena, on the other hand. The defects include point defects<sup>32-47</sup>, cluster defects<sup>32-47</sup> and boundaries or edges<sup>48-58</sup>, which also behave like defects in lowering the symmetry of the infinite crystal.

Point defects occur predominantly within the graphene plane in the form of lattice vacancies and impurity atoms<sup>1-25</sup>. The occurrence of impurities can be either in substitutional or interstitial sites and can be in the form of isotopic impurities<sup>17-25</sup>, which predominantly perturb the phonon spectra. Impurities in the form of foreign species (dopants) tend to mainly introduce local electric fields and strain fields associated with their local charge because of the small size of carbon atoms relative to all other species<sup>1-25</sup>. Boron, which is even smaller in size than carbon, is a special impurity atom that constitutes a common *p*-type dopant for graphene. Nitrogen, being larger than carbon, does not dope graphene as readily as boron but would be more likely to enter the lattice of narrow few layer graphene ribbons than bulk graphite. However, the solubility of both, boron and nitrogen in graphene is relatively low (< 2 at. %) <sup>1-16</sup>.

Hydrogen or fluorine tend to either physisorb in molecular form on specific graphene defect sites or to form graphane (hydrogenated graphene)<sup>72</sup>, and fluorinated graphene when added covalently and in high concentrations<sup>73,74</sup>. Generally speaking, the graphene structure forms well-ordered lattices, especially on epitaxial substrates, such as copper (111) or BN, and is relatively inert. When left in an ambient environment, oxygen and nitrogen molecules could be adsorbed on the graphene basal plane and relatively high annealing temperatures (800 °C)

are needed to desorb such molecules<sup>1</sup>. The naturally occurring vacancy concentration is determined by the growth temperature, which in turn is related to the growth method. Increasing the growth temperature reduces the naturally occurring vacancy concentration. The introduction of impurities is further discussed in connection with the chemical or electrochemical doping of graphene<sup>2,18,26,27,30,31,75-78</sup>. Ion implantation has been another common technique used for the introduction of point defects under controlled conditions by varying the ion species dose and ion energy<sup>33,34,58,79,80</sup>.

Graphene also accommodates two common types of carbon cluster defects with environments locally perturbed from the perfect *sp*<sup>2</sup> hybridized carbon<sup>32-47</sup>. The most common cluster defect is the 5-7-7-5 Throrer-Stone-Wales defect (Fig. 1a), but also frequently occurring are the 5-8-5 defects (Fig. 1b), both of which maintain an average of the six-carbon planar rings of graphene, and therefore graphene can be annealed at sufficiently high temperatures to lower its defect concentration. Since the 5-7-7-5 and 5-8-5 defects are symmetry-breaking, they can be observed spectroscopically in the Raman D-band (~1350 cm<sup>-1</sup> at 2.41 eV laser excitation), but the defects invoke other symmetry-breaking spectroscopic features, such as the D'-band at 1620 cm<sup>-1</sup> and combination modes such as the Raman D+G band 2930 cm<sup>-1</sup>, each with a different dispersion with laser excitation energy  $E_L$ <sup>1,2,32-47</sup>.

At present there is no clear information available on the use of the D-band lineshape, linewidth, laser energy dependence to quantitatively discriminate between the density of 5-7-7-5 and 5-8-5 defects/μm<sup>2</sup> in actual graphene samples, or between defects occurring in graphene samples prepared by different growth techniques. For the structural observation of individual isolated 5-7-7-5 and 5-8-5 defects, the TEM operated under high-resolution conditions, including aberration correction is especially powerful, especially for its ability to observe such individual defect clusters, or as either aggregated clusters or defect clusters in grain boundaries. *In situ* annealing studies of such defects in a dedicated environmental chamber under high-resolution conditions

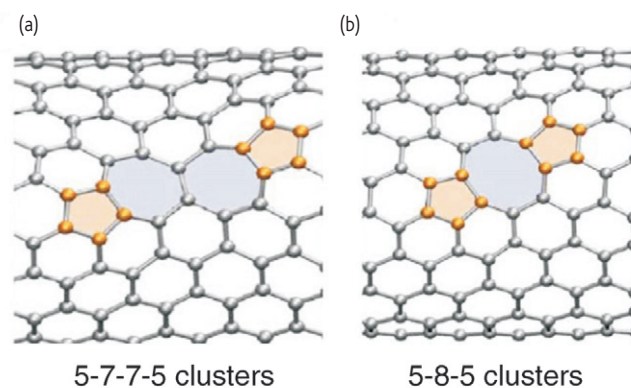


Fig. 1 Molecular models representing: (a) the 5-7-7-5 Throrer-Stone-Wales defect and (b) the 5-8-5 vacancy-like cluster defect. Because these defects maintain an average of the six carbon atoms per polygon in the graphene lattice, they can be annealed at sufficiently high temperature. Reprinted with permission from<sup>32</sup>. © 2006 by the American Physical Society.

would be rewarding to study the effect of each symmetry-breaking mechanism. The ability to do combined tip-enhanced Raman and TEM studies on the same physical cluster defect could provide unique information about the dynamics of such defects and the changes of the different vibrational modes. Recently, highly informative combined Raman and TEM studies on the same sample have been proposed and discussed<sup>4</sup>.

## Characterization of defects

As explained above, defects in graphene-like materials including carbon nanotubes can naturally arise from imperfections and growth-induced defects. These systems can even show defects that are artificially introduced to fulfill some needs for technological applications. In this section, we discuss promising techniques used to characterize defects in graphene-like systems.

## Micro-Raman spectroscopy

### Characterization of in-plane defects

Among several characterization techniques, micro-Raman spectroscopy (MRS) has been a powerful and widely used technique to study defects in carbon-based materials. Indeed, MRS is readily accessible, fast, non-destructive and gives a wealth of information about both the electronic and phonon structures of materials<sup>1,2,58</sup>. Particularly special, carbon-based materials show a very characteristic Raman feature called the D-band (the D denoting disorder-induced), which is a symmetry-breaking Raman peak that has no intensity in the absence of defects. Every time a given impurity breaks the translational symmetry of the carbon material's lattice, D-band intensity will appear in the Raman spectrum and its Raman cross-section ( $\sigma$ ) will be proportional to the defect concentration<sup>1,2,33,34,53,54,58</sup>. It is worth noting that not only can the D-band feature be used to understand defects in carbon materials, but also the symmetry allowed G-band and G'- (2D) band in the Raman spectra provide valuable information about defects especially when the impurity in question dopes the material by changing the bonding strength of the atomic species to the host carbon atoms.

Back in 1970, Tuinstra and Koenig<sup>81</sup> showed that the ratio between the D- and G-band Raman intensities ( $I_D/I_G$ ) is directly related to the crystallite size ( $L_a$ ) of 3D graphite. At that time, they explained their findings for only one excitation laser energy ( $E_L$ ), namely, 514 nm (2.41 eV). More than 30 years later, in 2006, Caňado *et al.*<sup>82</sup> successfully extended Tuinstra and Koenig's findings to several  $E_L$  values and now the ratio  $I_D/I_G$  is more fully described by the equation:

$$\frac{I_D}{I_G} = L_a \frac{E_L^4}{560} \quad (1)$$

where  $L_a$  is given in nm,  $E_L$  is given in eV and the constant 560 is given in units of eV<sup>4</sup>/nm. Although a general equation appeared through this scenario, a basic question still remained: whether the crystallite size  $L_a$  is a very special characterization parameter in graphite or would other

types of symmetry-breaking features also follow a similar equation? The answer is, not exactly.

In 2010, Lucchese *et al.*<sup>33</sup> used Raman scattering to study disorder in graphene caused by low energy (90 eV) Ar<sup>+</sup> ion bombardment. By varying the ion dose, the authors studied different densities of defects induced by the ion bombardment and were able to understand the evolution of the ratio  $I_D/I_G$  with ion dose (see Fig. 2). With this experiment the authors provided a Raman spectroscopy-based method to quantify the density of defects in graphene, using HOPG (highly oriented pyrolytic graphite) for calibration. In Fig. 2 the density of defects due to different ion doses is probed by  $L_D$ , which denotes the average distance between defects. This study revealed important information about the defect evolution by observing that  $I_D/I_G$  could be fitted by a phenomenological model for  $I_D/I_G$  vs.  $L_D$ . The model considers that the impact of a single ion in the graphene sheet causes modifications on two length scales, here denoted by  $r_A$  and  $r_S$  (with  $r_A > r_S$ ), which are the radii of two circular areas measured from the impact point (the subscript A stands for "activated" whereas the subscript S stands for "structurally-defective"). Qualitatively speaking, only if the Raman scattering process occurs at distances smaller than  $|r_A - r_S|$ , will the corresponding "damaged" region contribute strongly to the D-band feature. Considering these assumptions in conjunction with statistical arguments, the  $I_D/I_G$  vs.  $L_D$  relation is given by<sup>33</sup>:

$$\frac{I_D}{I_G} = C_A \frac{r_A^2 - r_S^2}{r_A^2 - 2r_S^2} \left[ e^{\frac{-\pi r_A^2}{L_D^2}} - e^{\frac{-\pi(r_A^2 - r_S^2)}{L_D^2}} \right] + C_S \left[ 1 - e^{\frac{-\pi r_S^2}{L_D^2}} \right] \quad (2)$$

where  $C_A$ ,  $C_S$ ,  $r_A$  and  $r_S$  are adjustable parameters. The model is in conceptual agreement with a well-established amorphization trajectory

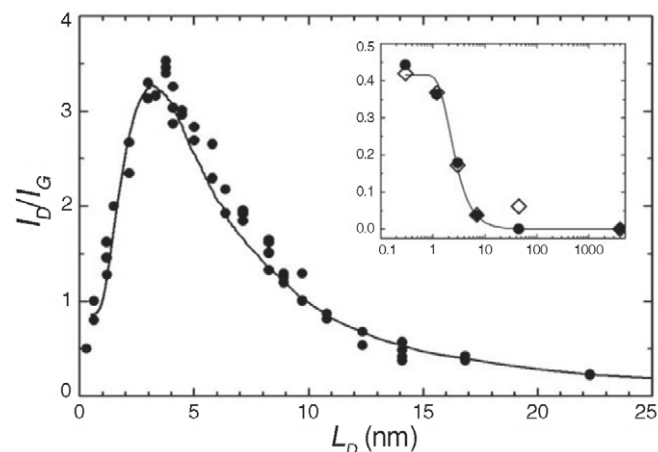


Fig. 2 The  $I_D/I_G$  data points from three different mono-layer graphene samples as a function of the average distance  $L_D$  between defects that are induced by the ion bombardment procedure. The inset shows the Raman intensity ratio  $I_D/I_G$  vs.  $L_D$  on a semilog scale for two graphite samples: (i) a ~ 50-layer graphene sample found near one of the three mono-layer graphene samples (bullets); (ii) a bulk HOPG sample used for calibration (diamonds). The bulk HOPG values in the inset are scaled by  $(I_D/I_G) \times 3.5$ . The solid line is obtained from Eq. 2, where  $C_A = (4.2 \pm 0.1)$ ,  $C_S = (0.87 \pm 0.05)$ ,  $r_A = (3.00 \pm 0.03)$  nm and  $r_S = (1.00 \pm 0.04)$  nm. Reprinted from<sup>33</sup> with permission from Elsevier. © 2010.

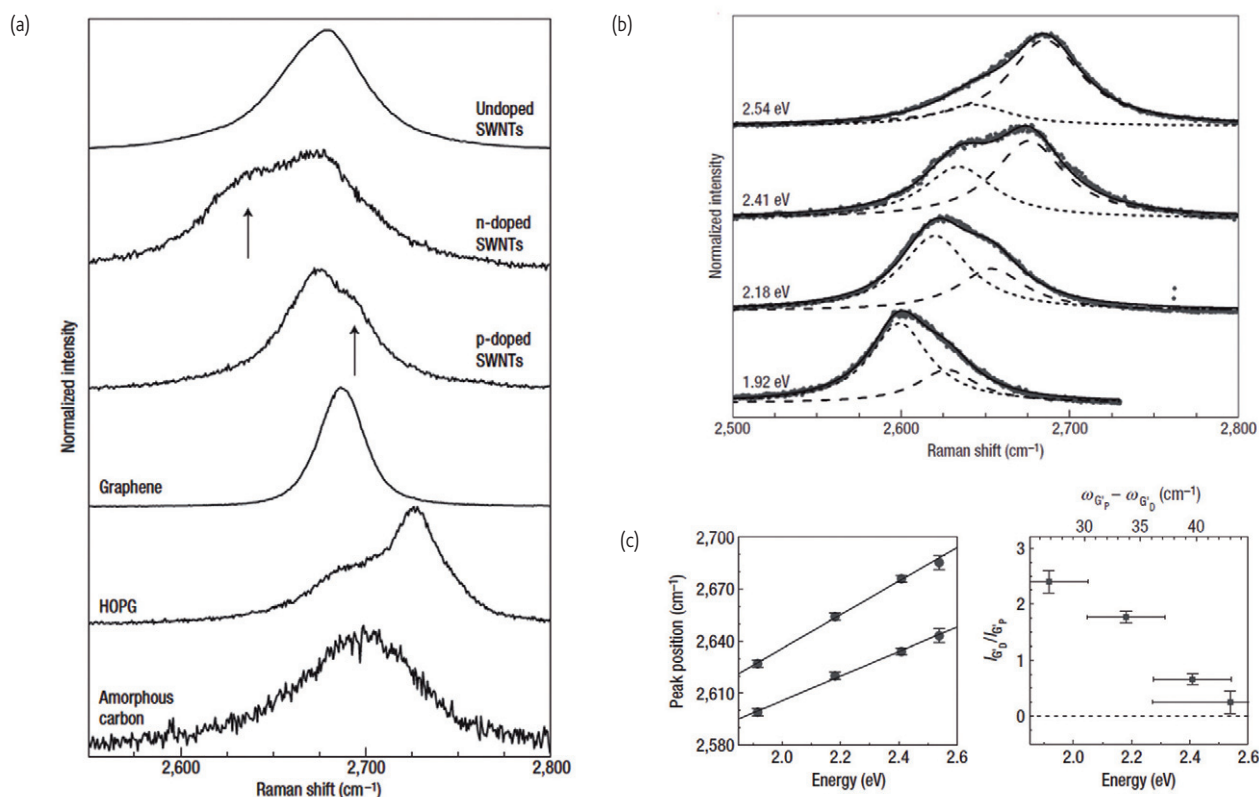


Fig. 3 (a) The arrows point to defect-induced peaks in the  $G'$ -band for doped SWNTs. The  $p/n$  doping comes from substitutional boron/nitrogen atoms, the nearest neighbors of carbon in the periodic table. The spectra of graphene, HOPG and amorphous carbon are shown for comparison. The spectra were measured at room temperature with  $E_L = 2.41$  eV (514 nm). (b) The  $G'(2D)$ -band spectra with different  $E_L$  for the  $n$ -doped SWNT sample. (c) The  $G'$  peak position as a function of  $E_L$ , obtained by fitting the spectra in (b) with two Lorentzians. The line width  $\gamma$  is determined by the full-width at half-maximum intensity and the values of each Lorentzian linewidth increases linearly with  $E_L$  from  $\gamma = 43$  to  $53$   $\text{cm}^{-1}$ . The solid lines are linear fits giving  $\omega_{G'_p} = (97 \pm 5)E_L + (2,442 \pm 11)$   $\text{cm}^{-1}$  and  $\omega_{G'_D} = (71 \pm 4)E_L + (2,465 \pm 11)$   $\text{cm}^{-1}$ . (d) The  $G'$ -band intensity ratio ( $I_{G'_D}/I_{G'_p}$ ) as a function of  $E_L$ . The upper scale gives the difference between the  $G'_p$  frequency ( $\omega_{G'_p}$ ) and the  $G'_D$  frequency ( $\omega_{G'_D}$ ). Here,  $G'_p$  stands for the undoped pristine  $G'$ -band, while  $G'_D$  stands for the doped  $G'$ -band. Reprinted from<sup>67</sup> by permission from Macmillan Publishers Ltd, © 2010.

for graphitic materials<sup>1,2,33,58</sup>. Additionally, the results show that the broadly used Tuinstra and Koenig relation between  $I_D/I_G$  and  $L_a$  should be limited to the measurement of 3D crystallite sizes. Recently, in 2011, Cañado *et al.* extended the proposed phenomenological model to be applicable to several laser lines<sup>34</sup>.

Other types of defects are those that dope the carbon material positively ( $p$ -type defects) or negatively ( $n$ -type defects)<sup>1-16</sup>, and those that introduce isotopic defects, the latter being neutral impurities that have only their atomic mass different from that of the pristine sample<sup>17-25</sup>. All these impurities can be naturally introduced into the carbon lattice by their substitution in the place of some original carbon atoms or by functionalization of the sample<sup>1-25</sup>. In the context of the MRS characterization of these functionalized impurities, a new analysis for the  $I_D/I_G$  ratio as a function of dopant concentration and  $E_L$  is still required in order to understand in depth the differences in connection with the use of Eq. 1. Experiments of MRS combined with x-ray photoelectron spectroscopy (XPS) to determine the amount of dopants could be carried out in order to correlate the D-band peak with the

dopant concentration. Therefore, additional combined measurement techniques are awaiting development.

However, it is interesting to note that, while for graphene, these chemical doping and functionalization procedures are still under development, for single-walled carbon nanotubes (SWNTs) such chemically modified samples have been available for a much longer time so that much is already known about how to understand some of the effects of such defects on the electronic and vibrational properties of SWNTs<sup>2</sup>. For substitutional  $n$ -type and  $p$ -type doping, it turns out that the  $G'(2D)$  band is extremely sensitive in discriminating between these two different types of doping impurities. More recently, Maciel *et al.*<sup>67</sup> showed that these impurities renormalize both the electronic and the vibrational structures of carbon nanotubes, and by analyzing the particular behavior of the  $G'(2D)$ -band in some doped carbon nanotubes, they could both distinguish between  $n$ -type or  $p$ -type doping as well as give information about the dopant concentration, as exhibited in Fig. 3.

Regarding defects due to the introduction of isotopes into SWNTs, Costa *et al.*<sup>17</sup> have shown how MRS also reveals special phenomena related

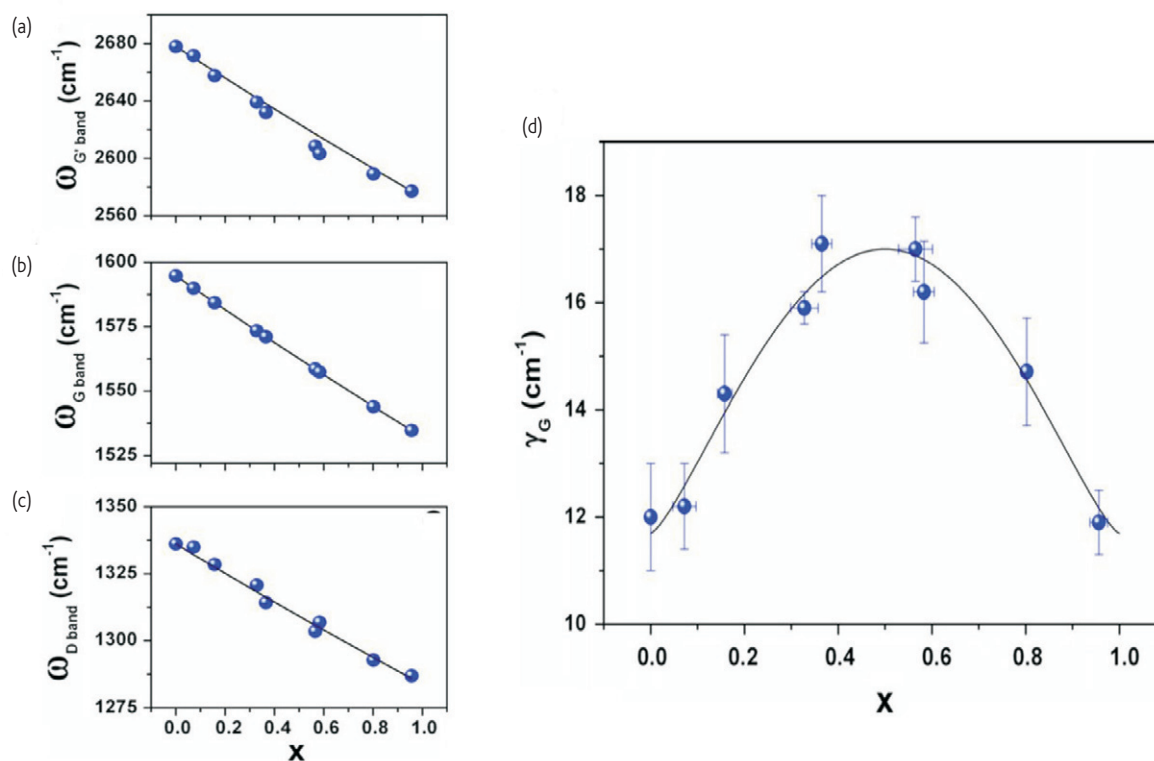


Fig. 4 (a) G'(2D)-band, (b) G-band, and (c) D-band frequencies as a function of the  $^{13}\text{C}$  content in the sample containing a  $^{13}\text{C}$ : $^{12}\text{C}$  ratio  $x$ . The circles represent experimental points and the solid lines are from model calculations. (d) The data shows a parabolic trend with its maximum at around  $x = 0.5$ , and its minima at  $x = 0$  and  $x = 1$ . Reprinted from<sup>17</sup> with permission from Elsevier. © 2011.

to isotopes, as shown in Fig. 4. The study reveals linear dependences of the Raman D-band, G-band and G'(2D)-band frequencies with an increase in the relative  $^{13}\text{C}$  concentration ( $x$ ) for each of these nanotube Raman modes, and shows that the effect of the mass variation of the isotope mixture on the phonon frequencies is described through a simple harmonic oscillator model involving  $^{13}\text{C}$  and  $^{12}\text{C}$  species. The solid lines in Figs. 4a, b, and c are fittings of the experimental data to such a harmonic oscillator model for

the frequency and linewidth. Finally, measurements with different  $E_L$  were performed and the frequency dispersions of the D and G'(2D)-bands with  $E_L$  were observed to be the same for  $^{12}\text{C}$  and  $^{13}\text{C}$  nanotubes, suggesting no changes in the electronic structure after isotope enrichment, in contrast to what happens for  $n$ -type and  $p$ -type impurities<sup>17</sup>.

It is worth mentioning that recent advances in the Raman spectroscopy of  $n$ -doped and  $p$ -doped graphene have been reported by

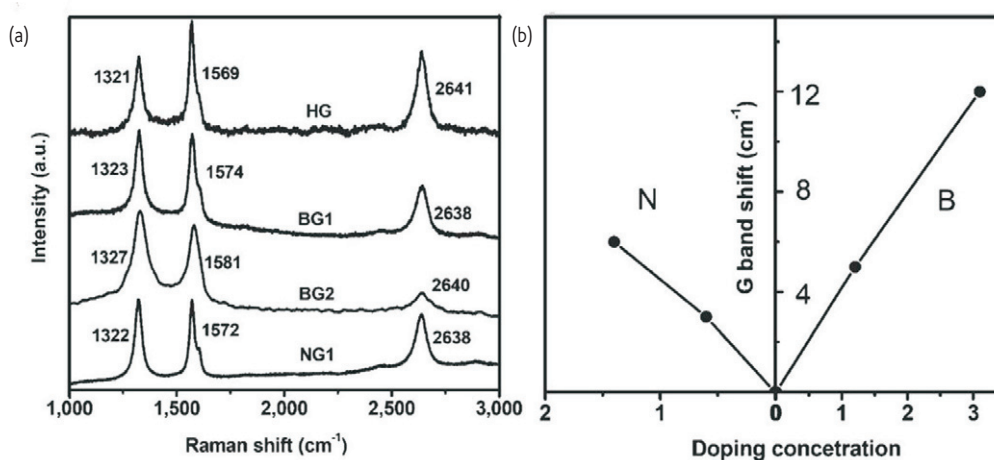


Fig. 5 (a) Raman spectra of undoped (HG), boron-doped (BG) and nitrogen-doped (NG) graphene samples. (b) G-band frequency shifts caused by electron (N) doping (with pyridine) and hole (B) doping. From an  $I_D/I_G$  analysis, it is concluded that the crystallite size is smaller for doped samples than for undoped ones. Reproduced from<sup>9</sup> with permission from John Wiley and Sons. © 2009.

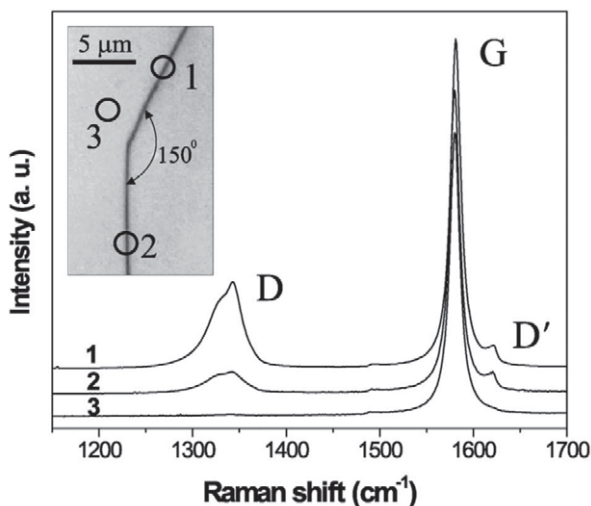


Fig. 6 Raman spectra obtained in three different regions of a HOPG graphite sample (open circles in the inset). Namely, the region 1 is an armchair edge, the region 2 is a zigzag edge, while the region 3 is bulk graphite. The spectra were taken at room temperature and the laser energy  $E_L$  was 1.96 eV. The inset shows an optical image of the edge regions. Reprinted with permission from<sup>53</sup>. © 2004 the American Physical Society.

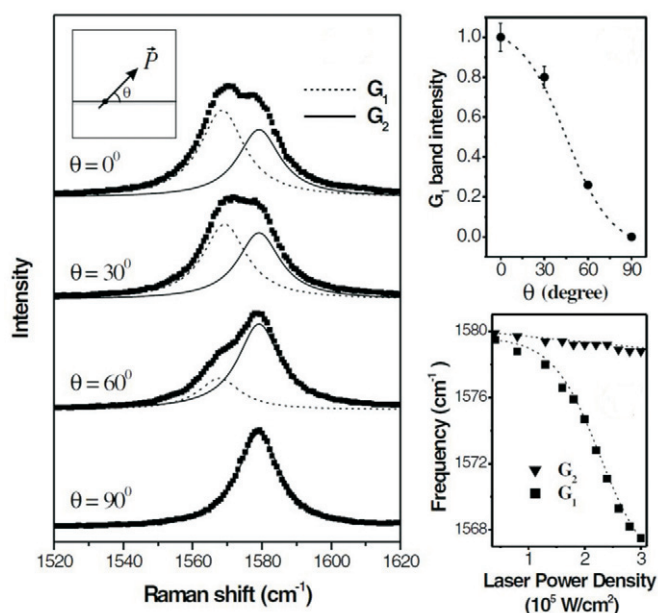


Fig. 7 (a) Raman spectra obtained for light incident with different polarization angles ( $\theta$ ) with respect to the ribbon direction. The inset shows a schematic figure of the sample (horizontal gray line) showing the direction between the ribbon axis and the light polarization vector. (b) Intensity of the ribbon's G-band ( $G_1$ ) peak versus  $\theta$  (note that  $G_2$  stands for the G-band of the bulk graphite substrate). The dotted line is a  $\cos^2\theta$  theoretical curve for the expected  $\theta$  dependences. The error bars are associated with baseline corrections. (c) Raman frequencies of the graphite substrates  $G_2$  (triangles) and the graphene ribbon  $G_1$  (squares) peaks as a function of the laser power density<sup>54</sup>. Thus, we observe that Raman spectroscopy can distinguish between graphene edges and bulk graphite, and that this technique can also distinguish zigzag edges from armchair edges through the dependence of the Raman intensity on the light polarization angle with respect to the ribbon axis. Reprinted with permission from<sup>54</sup>. © 2004 the American Physical Society.

Panchakarla *et al.*<sup>9</sup>. The impurities in this case are naturally introduced during the growth process and are, therefore, mainly substitutional. Their results can be summarized in Fig. 5. Basically these authors report an asymmetric phonon renormalization of the G-band feature in which defects due to  $n$ -type and  $p$ -type both result in a frequency upshift (note that the impurity concentration only changes the renormalization factor). This hardening of the G-band is explained by means of the phonon self-energy in graphene within the non-adiabatic formalism, and its broadening is due to the absence or blockage of the decay channels of the phonons into electron-hole pairs<sup>83</sup>. However the upshift rate is larger for  $p$ -doped samples in comparison to the  $n$ -doped ones. From an  $I_D/I_G$  analysis, these authors were able to find that the crystallite size  $L_a$  for doped graphene is smaller than  $L_a$  for undoped graphene, which is expected because of the extra strain introduced by the dopants compared to the strain in a pristine sample.

### Characterization of armchair and zigzag edges

For graphene nanoribbons, edges can be considered to be symmetry-breaking discontinuities. Here, AC-HRTEM (aberration-corrected high resolution transmission electron microscopy) can be used directly to identify the edge type. Since the zigzag edges have a high density of electronic states relative to other edge types<sup>57</sup>, polarized Raman spectroscopy can be used to distinguish zigzag edged ribbons from ribbons with armchair and chiral edges, as shown in Fig. 6<sup>53</sup>.

Since the Raman tensor for the zigzag ribbons causes the Raman cross-section to vanish for the optical electric field polarization of light parallel to a zigzag edge, Raman spectroscopy can also be used to distinguish zigzag nanoribbons from ribbons from other edge types, as shown in Fig. 7, in which the Raman spectra were obtained for light incident with different polarization angles ( $\theta$ ) with respect to the nanoribbon direction for a narrow graphene ribbon sitting on a bulk graphite substrate<sup>54</sup>.

After this brief discussion about MRS and its applications for the characterization of defects, it is important to note that MRS provides us with information about defect concentrations, crystallite sizes and property changes due to  $n$ -type and  $p$ -type doping, including similarities and differences. However, MRS cannot tell us by itself the structural differences of, for example, the type of defect which breaks the translational symmetry (vacancies or dopants). MRS cannot tell us if the vacancies are point vacancies or 5-7-7-5 or 5-8-5 defect clusters. Moreover, MRS cannot provide precise information if a given impurity atom is  $n$ -type,  $p$ -type, substitutional, or interstitial. For these purposes other observation techniques such as TEM, STM, or near-field spectroscopy would also be required.

### Tip-enhancement near-field spectroscopy

Tip-enhancement Near-field spectroscopy (TES) is a technique that combines both: atomic force microscopy (AFM) and confocal optical microscopy. This special combination of techniques provides,

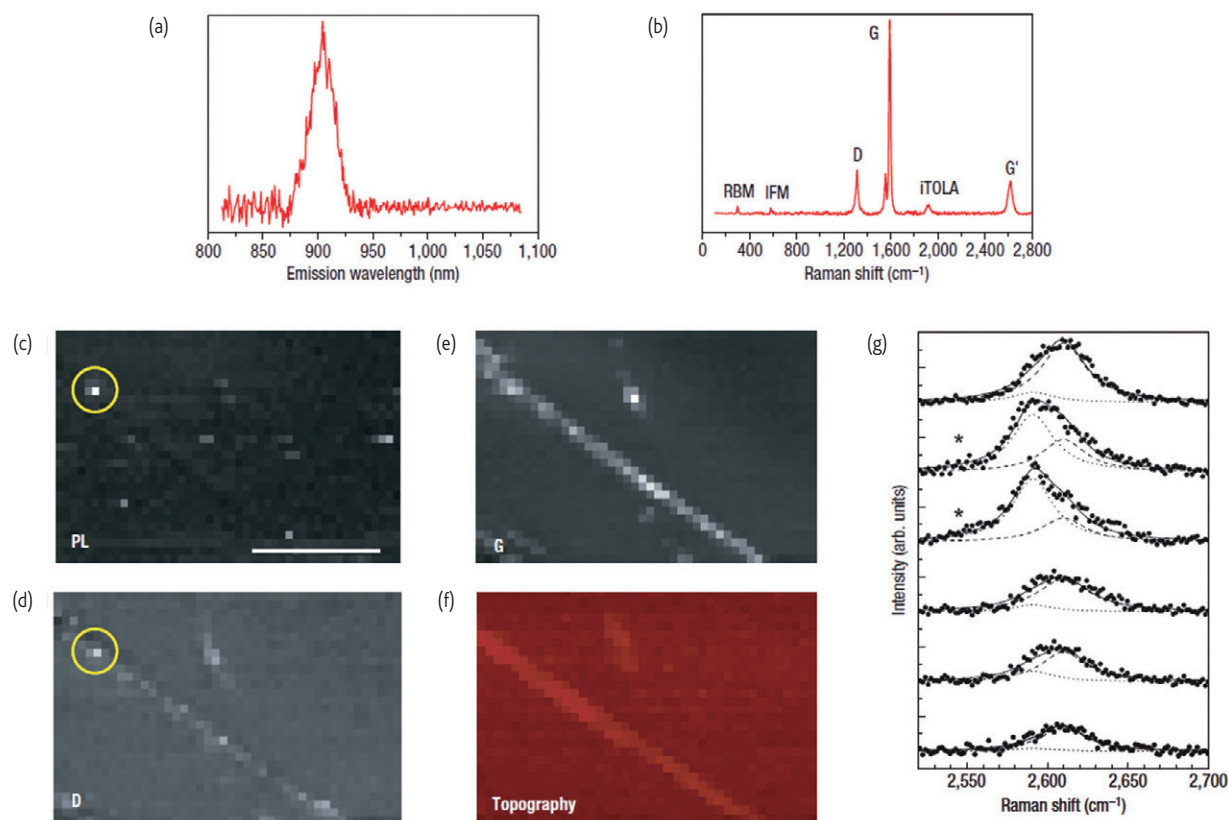


Fig. 8 Near-field Raman and photoluminescence spectroscopy and imaging of a (9, 1) SWNT with  $E_L = 1.96$  eV (633 nm). (a) Photoluminescence emission at  $\lambda = 904$  nm. (b) Raman spectrum in which the main Raman features are labeled. (c) Near-field photoluminescence image of the SWNT revealing localized excitonic emission. The scale bar denotes 250 nm. (d) and (e) show the near-field Raman imaging of the same SWNT, where the image contrast is provided by spectrally integrating over the tangential G-band (d) and defect-induced D band (e). (f) Corresponding topography image. (g) Evolution of the G'-band spectra near the defective segment of the (9, 1) SWNT. The spectra were taken in steps of 25 nm along the nanotube, showing the defect-induced  $G'_D$  peak (dotted Lorentzian). The asterisks (\*) denote the spatial locations where localized photoluminescence and defect-induced D band scattering were measured (see yellow circles in (c) and (e), respectively). The  $\omega_{G'P} - \omega_{G'D}$  splitting observed in (g) is smaller than the splitting observed in Fig. 3(b) because the spectra were measured with different excitation laser energies, as discussed in reference<sup>67</sup>.

simultaneously, sub-wavelength and high spatial resolution of samples (determined exclusively by the diameter of the metallic tip used in the experiment) resulting in a wealth of information at the atomic scale<sup>68, 69</sup>. Similar to MRS, TES cannot provide information regarding the type of defects that are connected to a given sample, or if the impurity atoms are substitutional or not. However, while MRS probes clusters of defects, TES allows us to determine individual impurities at near atomic resolution, which in most cases reveals the different local interactions of impurities with the pristine material.

Maciel *et al.*<sup>67</sup> also showed that TES can selectively excite regions with and without defects along individual carbon nanotube structures, as shown in Fig. 8. It is shown that TES experiments can be used to understand the local differences (in relation to the pristine material) generated by *n*-type and *p*-type dopants. As explained in the last section, the  $G'(2D)$  feature measured by MRS consists of two peaks: one is related to the dopants and another, related to the pristine contributions, is shifted in frequency from the first peak. Similarly to Qian *et al.*<sup>69</sup>, in the work by Maciel *et al.*<sup>67</sup> the

authors could discriminate the optical responses of regions with and without impurities, and by comparing the observed Raman and photoluminescence signals, they clearly could see a localized photoluminescence emission coming from the defective site. However, the work of Maciel *et al.*<sup>67</sup> showed that every time the tip was standing over a defective region, the Raman signal from both the defect and from the pristine nanotube were observed, while only the pristine nanotube signal was observed in regions without a defect. This is an expected result because the Raman signal is strongly connected with the polarizability of the material and therefore the observed spectra will reflect both the electronic and vibrational structure of the material, while photoluminescence is sensitive basically to changes in the electronic structure.

Another application of TES is the length scale study of defect-induced Raman modes in carbon materials. Recently, Georgi and Hartschuh<sup>70</sup>, successfully applied TES to investigate with high spatial resolution the D-band scattering near defects in metallic SWNTs. In their work, Georgi and Hartschuh found that the length scale of the D-band scattering

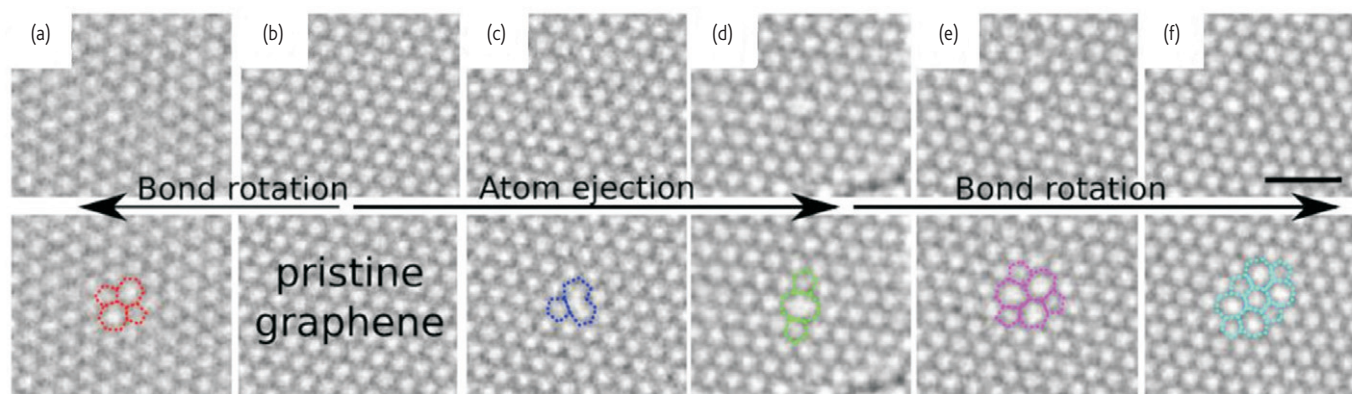


Fig. 9 Elementary defects and frequently observed defect transformations under irradiation. Atomic bonds are superimposed on the defective areas in the bottom row. The creation of the defects can be explained by atom ejection and reorganization of bonds via bond rotations. (a) The Thrower-Stone-Wales defect, (b) defect-free graphene, (c) (5-9) vacancy, (d) (5-8-5) divacancy cluster, (e) (555-777) divacancy cluster, (f) (5555-6-7777) divacancy cluster. Scale bar is 1 nm. Reprinted with permission from<sup>35</sup>. © 2011 by the American Physical Society.

process is about 2 nm in SWNTs, similar to this length in graphene<sup>84</sup>. It is worth emphasizing that this 2 nm length is also a value for  $L_D$  obtained from ion implantation studies<sup>33</sup>.

### High resolution transmission electron microscopy

Aberration-corrected AC-HRTEM is highly effective for studying the morphology of carbon based materials<sup>1,35,36,59-63</sup>. Of course, AC-HRTEM has the advantage of high (atomic scale) resolution so that it provides valuable information about the atomic structure of pristine materials as well as the impurities in defective materials. This technique has the disadvantage of requiring expensive equipment, is time-consuming in operation and, most of time, AC-HRTEM is destructive in the sense that one cannot be assured that the sample will keep its same characteristics before and after the HRTEM analysis. Another drawback of this technique is that it relies on additional complex and dedicated equipment that is needed to extract useful information from the images<sup>1,35,36,59-63</sup>. AC-HRTEM would be ideal to fully characterize, for example, 5-7-7-5 and 5-8-5 defects in nanocarbons<sup>1,35,36,59-63</sup>. Because this is currently a widely discussed topic in the literature, we will restrict our attention to recent results involving HRTEM techniques<sup>35,36</sup>.

Recently, Kotakoski *et al.*<sup>35</sup> used electron irradiation to create a  $sp^2$ -hybridized one-atom-thick flat carbon membrane with a random arrangement of polygons (in other words: a graphene sheet containing heptagons, hexagons and pentagons that resembles the pentaheptite<sup>85</sup> and Haeckelite-like structures<sup>86</sup>). The authors demonstrate, by means of first principles calculations and AC-HRTEM experiments how the transformation occurs step by step by nucleation and growth of low-energy multivacancy structures constructed from rotated hexagons and other polygons (see Fig. 9). The observations in this work<sup>35</sup> provide new insights into the bonding behavior of carbon and the dynamics of defects in graphene. It would therefore be ideal to perform *in situ* Raman spectroscopy measurements on the different types of defective graphenes.

Another interesting application also involving AC-HRTEM is presented by Meyer *et al.*<sup>36</sup>. They demonstrate an experimental analysis of charge redistribution due to chemical bonding in nitrogen-doped graphene membranes and boron-nitride monolayers. Namely, the electronic charge density distribution of a solid contains information about the atomic structure and also about the electronic properties, such as the nature of the chemical bonds or the degree of ionization of atoms. This work turns out to be important because the redistribution of charge due to chemical bonding is small compared with the total charge density and is difficult to measure. Although the differences are small, a full understanding of how this charge redistribution works is needed. In other words, the electron scattering by a carbon atom next to a nitrogen atom turns out to be significantly different from electron scattering by a carbon atom elsewhere in the graphene sheet.

The success of Meyer *et al.* relies on AC-HRTEM measurements of defective sites in graphene. In this way, they correct the spherical aberrations of the microscope and do a defocus large enough so that in the contrast transfer function (CTF), features from the nitrogen can be distinguished from the carbon atoms. In order to explain the experiment they use first principles modeling techniques, considering the charge redistribution everywhere the nitrogen atom is located. In this context, they also show that the traditional independent atom model (IAM) analysis is inappropriate to properly interpret HRTEM results in defective samples. Fig. 10 shows a comparison between the two methods of analysis and their consequences on the simulated HRTEM images. Note that in Fig. 10c it is seen that, no matter what is the defocus status, if one uses the IAM, the nitrogen atom cannot be distinguished. However, in Fig. 10f, especially for the defocus status  $f/2$ , it is possible to clearly observe the effects of the hydrogen atom in the graphene lattice.

With this combination of techniques, the authors analyzed the charge transfer on the single-atom level for nitrogen-substitution point defects in graphene, and they confirm the ionicity of single-layer hexagonal boron nitride. Moreover, it is possible to obtain insights into the charge distribution in general nanoscale samples and non-periodic defects can



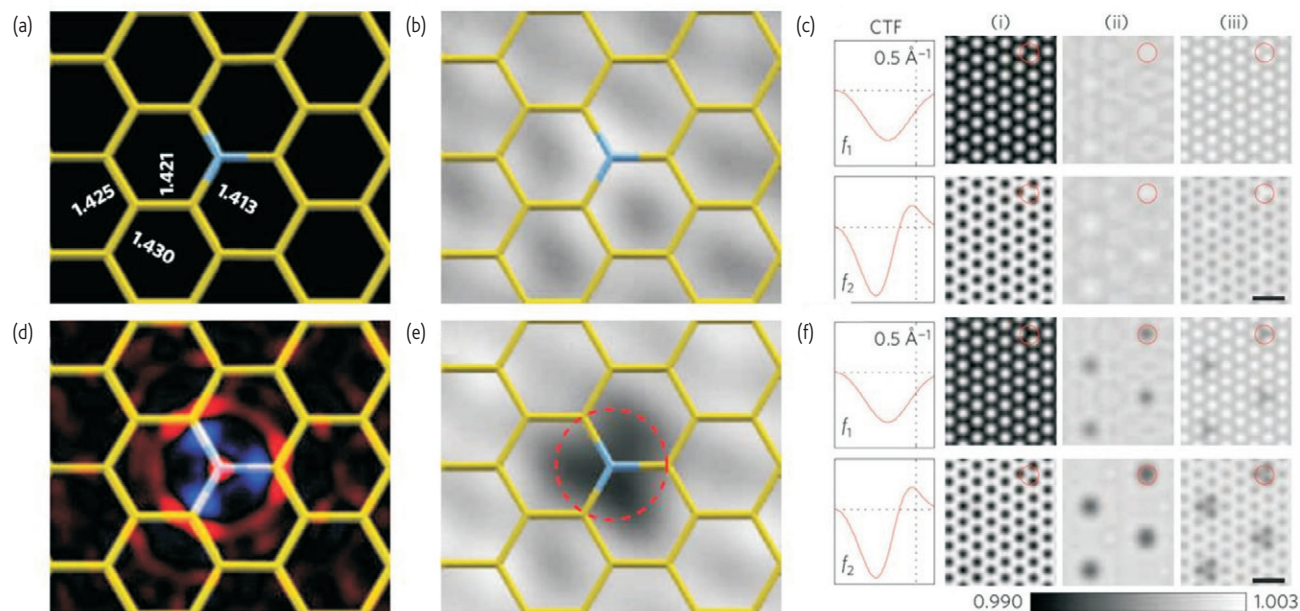


Fig. 10 Charge distribution, projected potentials and TEM simulations for nitrogen-doped graphene. (a) The relaxed atomic configuration for a nitrogen impurity substitution in graphene. Bond lengths are given in angstroms. (b) Projected potential based on the IAM (independent atom model), with the periodic components of the graphene lattice removed, and bandwidth-limited to their experimental resolution (about  $1.8 \text{ \AA}$ ). Dark contrast corresponds to higher projected potential values, in accordance with conventional TEM imaging conditions. (c) TEM simulation based on the IAM potential, for two different defocus parameters  $f_1$  and  $f_2$ , where the condition  $f_2$  stands for a more defocused situation. Filters are: (i) unfiltered, (ii) periodic components removed by a Fourier filter, and (iii) low-pass filtered. (d) Atomic structure (using the same bond lengths), with the changes in the projected electron density due to bonding shown in colour. Blue corresponds to a lower, red to a higher electron density in the DFT result as compared with the neutral-atom (IAM) case. (e) Projected potential, filtered as in (b), based on the all-electron DFT calculation. (f) TEM simulations using the DFT-based potentials. The grey-scale calibration bar applies to columns (ii) and (iii), which are all shown on the same grey-scale range for direct comparison. The scale bars are  $5 \text{ \AA}$ . Reprinted from<sup>36</sup> by permission from Macmillan Publishers Ltd, © 2011.

be clearly observed in HRTEM measurements. They have shown that HRTEM experiments when used with first-principles electronic structure calculations opens a new way to investigate electronic configurations of point defects and other non-periodic arrangements of nanoscale objects that cannot be studied by a conventional electron or x-ray diffraction analysis. Moreover, this approach is also very promising for studying vacancy cluster defects, since the existence of vacancies will also require a local redistribution of charge densities. In the future, AC-HRTEM coupled with MRS or TES need to be developed. In this way a clear understanding of the vibrational modes associated with different types of point defects can be achieved. In addition, theoretical calculations indicating the Raman modes associated with the different types of defects still need to be performed. An impressive example of the use of AC-HRTEM to resolve details of grain boundary defects in graphene is shown in Fig. 11 where pentagons (blue), heptagons (red) and distorted hexagons (green) can be seen<sup>87</sup>. Here, variants of Thrower-Stone-Wales defects can be directly identified.

Finally, it is worth mentioning that layer stacking defects have also been recently investigated by both AC-HRTEM and optical techniques. In the case of trilayer graphene, the closest packed Bernal ABA stacking is most commonly observed, though ABC rhombohedral stacking has also been identified and investigated<sup>88–90</sup>. Since the HRTEM analysis can

directly distinguish between ABA and ABC stacking because of the well identified structural stacking differences, this technique is used as a primary standard for the structural identification of graphene samples. Once optical techniques that can also distinguish between these stacking arrangements are established, these more commonly available optical techniques can become secondary laboratory methods for identifying the various structural arrangements that occur commonly in few layer samples<sup>88–90</sup>.

### Other techniques

Besides the techniques presented above, it is worth mentioning that some other approaches (perhaps less well-known or even too new to be known) could be chosen to understand more about the nature of defects. In this context, scanning tunneling microscopy (STM) and spectroscopy (STS) constitute non-destructive techniques that reveal a wealth of information about the electronic structure of carbon materials as well as their impurities<sup>1,64–66</sup>. An STM in its basic mode of operation will stabilize a sharp metallic tip about  $1 \text{ nm}$  above the materials surface. In this situation, an electron can tunnel from the tip to the sample and vice versa. Therefore, any tunneling current variation will be related to the density of states in the surface of the material under study, which reveals details about the material's electronic structure. It is worth noting that transport measurements are also powerful for revealing details of the

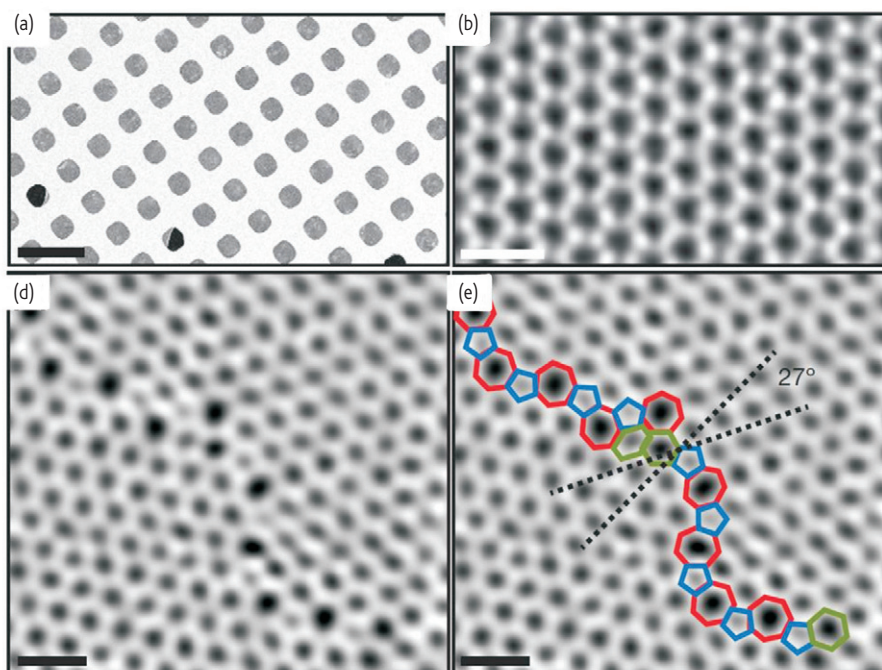


Fig. 11 Atomic-resolution AC-HRTEM images of graphene crystals. (a) Scanning electron microscope image of graphene transferred onto a TEM grid with over 90% graphene coverage. Scale bar, 5 mm. (b) AC-HRTEM image showing the defect-free hexagonal lattice inside a graphene grain. (c) Two grains (bottom left, top right) intersect with a  $27^\circ$  relative rotation angle, where an aperiodic line of defects stitches the two grains together. (d) The image from (c) with the pentagons (blue), heptagons (red) and distorted hexagons (green) of the grain boundary outlined. (b)-(d) were low-pass-filtered to remove noise; scale bars,  $5\text{ \AA}$ . Reprinted from<sup>87</sup> by permission from Macmillan Publishers Ltd, © 2011.

electronic structure of graphene-like materials. Indeed, because the electronic transport is crucial to develop industrial applications, one has to understand how devices (such as transistor and sensors) based graphene-like materials will behave in the presence of dopants<sup>75, 76, 77</sup> and/or structural defects<sup>79,80</sup>.

Gate-modulated Raman spectroscopy is another technique that has been extensively used in the field of nanocarbon materials. As an important example, the isotope effect has been exploited to study the effect of the interaction of a graphene layer with a  $\text{SiO}_2$  substrate<sup>18</sup>. In their work, Kalbac *et al.*<sup>18</sup> prepared two samples containing a single  $^{13}\text{C}$  layer ( $^{13}\text{C}$  1-LG). In one case, a single  $^{13}\text{C}$  layer is in contact with the  $\text{SiO}_2$  substrate. The Raman spectrum of this sample is then compared with both a similarly prepared mono-layer  $^{12}\text{C}$  sample ( $^{12}\text{C}$  1-LG) on a similar  $\text{SiO}_2$  substrate and the Raman spectrum from a bilayer sample ( $^{13}\text{C}/^{12}\text{C}$ -LG) composed of a single layer of  $^{12}\text{C}$  on a  $\text{SiO}_2$  substrate on top of which a single layer of  $^{13}\text{C}$  is deposited to form the bilayer. In this latter case the two layers of the bilayer graphene are turbostratically arranged. Raman spectra of these three samples taken at a laser energy  $E_L = 2.33\text{ eV}$  are shown in Fig. 12.

Here the frequency  $\omega$  of the  $^{13}\text{C}$  Raman line is down shifted relative to that labeled by  $\omega_0$  coming from  $^{12}\text{C}$  according to the relation  $(\omega_0 - \omega)/\omega_0 = 1 - [(12 + c_0)/(12 + c)]^{1/2}$  in which  $c = 0.99$  is the  $^{13}\text{C}$  concentration in the  $^{13}\text{C}$ -enriched sample and  $c_0 = 0.0107$  is the natural abundance of  $^{13}\text{C}$  in the naturally occurring carbon material. Using electrochemical techniques these authors varied the Fermi level

from  $-1.5\text{ V}$  to  $+1.5\text{ V}$  in steps of  $0.1\text{ V}$  using a calibrated reference potential where the  $V = 0$  potential corresponds to that of the  $^{13}\text{C}$  layer which is deposited on the  $^{12}\text{C}$  layer of the bilayer graphene sample, and electrochemical Raman results on the G band and on the G' band were obtained<sup>18</sup>. Since gating has become a very important technique for changing the Fermi level in both graphene and SWNTs, the use of electrochemistry for providing calibration standards is important. Electrochemical measurements allow calibration of frequency upshifts for positive potentials and frequency upshifts for negative potentials. That upshifts in frequency occur for both positive and negative potentials is consistent with the chemical doping experiments of Maciel *et al.*<sup>67</sup>.

The authors would like to mention that doping techniques to study the electron-phonon coupling in  $^{12}\text{C}$  graphene systems have been extensively used in the literature<sup>91-93</sup>. Finally, transport measurements, optical absorption, photoluminescence, thermo-gravimetric analysis and thermal-transport measurements could also indirectly reveal and quantify defects (impurities) by scanning a structure containing a well-identified defect<sup>1,39,58</sup>.

It is noteworthy that the methods to identify, quantify and detect defects discussed here, could be applied to other carbon nanosystems, but some adjustments might be necessary. For example, graphite and graphene are similar systems but their defect detection and quantification, using the techniques above, cannot be simply extrapolated. Raman spectra as well as HRTEM data would be different and defect formation due to ion irradiation needs adjustments and further research along

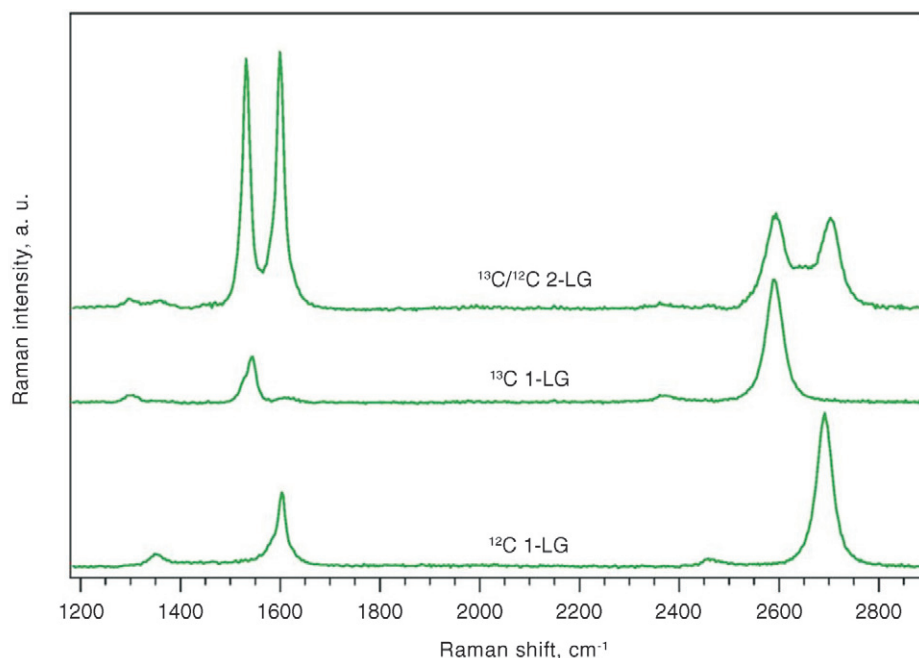


Fig. 12 Raman spectra of the  $^{12}\text{C}$  1-LG,  $^{13}\text{C}$  1-LG, and  $^{13}\text{C}/^{12}\text{C}$  2-LG ( $^{13}\text{C}$  is on top,  $^{12}\text{C}$  at bottom) samples on  $\text{SiO}_2$  substrates. The spectra are excited using  $E_L = 2.33$  eV laser excitation energy. Reprinted with permission from<sup>18</sup>. © 2011 American Chemical Society.

these lines is still needed. A similar scenario is observed for single- and multi-walled carbon nanotubes. Therefore, the present review is also intended to provide carbon researchers with valuable information related to defects and impurities that could be used and adapted to other systems including carbon foams, graphene oxide, nanotubes, etc., but significant further research would be needed to properly characterize heavily irradiated carbons and highly disordered carbons.


## Conclusions and perspectives

In this review article we discussed a variety of defects and impurities in graphene-like materials, including their structure, properties, characterization and application. By envisioning real applications for these structures, one must consider that the material at the same time will somehow become degraded by defects or impurities. As discussed throughout the text, defects such as *n*-type or *p*-type dopants, isotopic substitutions and defect clusters (5-7-7-5 or 5-8-5) could be found in nano-carbons and intermolecular junctions, and are also naturally abundant. In the section *Types of defect* we discussed the nature of such defects and how they occur. Among the many characterization techniques currently available, our discussion in the section *Characterization of defects* focused on the more promising techniques now used to characterize and understand defects. Despite its limitations to distinguish between defects as well as to probe them individually, MRS remains a fast and widely accessible tool which provides a fair understanding of the electronic and vibrational properties of materials. In contrast to MRS are electron microscopy techniques, particularly AC-HRTEM. While, HRTEM is unique in several aspects, its most striking feature is its ability to probe

in depth the nature of atomic bonding in crystals. Thus, HRTEM allows for a detailed identification of how specific types of defects occur in materials and how they locally change the material's properties. Other characterization techniques were also briefly discussed, such as scanning probe microscopy (STM, AFM, and others), which greatly amplify our understanding of the electronic properties of materials surfaces.

There had been little attention given to the study of defects in nanostructures and this is because the synthesis of large-scale nanostructures with only a few naturally occurring defects has been difficult. Therefore emphasis has historically been given to promoting the synthesis of defect-free structures with high electronic mobilities and for the scale-up of such structures to the micron and even centimeter length scales for potential practical applications. Now that much progress has been made in materials preparation and characterization, it is time to take stock of where we are now, where we are going in the future, and what scientific barriers remain to be overcome. Among the scientific barriers to future progress is the controlled introduction of defects in the growth process, including point defects, cluster defects and grain boundaries, with grain boundaries arising in the growth process because of the different nucleation sites for graphene grain growth.

Finally, although the topic was not mentioned in the manuscript, the authors believe in the use of defects in applications such as for providing specific sensor sites for molecular adsorption. Enhancing the performance of the different kinds of sensor sites that can now be developed, by increasing the density of such available sites and by expanding the number of ways that such sensor sites could be used reliably and the promotion of new large-scale applications should be emphasized but special niche applications

could also be a good strategy for developing technological tools. Carbon, like silicon, is an abundant and cheap element on our planet. Therefore its use for large scale applications is desirable and could perhaps become part of global sustainability planning if graphene and other nanocarbons could be conveniently and cheaply synthesized from CO<sub>2</sub> or waste CH<sub>4</sub>. 

## Acknowledgements

PTA acknowledges financial support from CNPq grant No.200616/2010-2. PTA and MSD acknowledge financial support from ONR-MURI-N00014-09-1-1063. MT acknowledges support from the Research Center for Exotic Nanocarbons, Japan regional Innovation Strategy Program by the Excellence, JST.

## REFERENCES

- Jorio, A., Dresselhaus, G., and Dresselhaus, M. S., *Carbon Nanotubes: Advanced Topics in the Synthesis, Structure, Properties and Applications*. Springer-Verlag, Berlin, (2008).
- Panchakarla, L. S., et al., *ACS Nano* (2007) **1**, 494.
- Koos, A. A., et al., *Carbon* (2010) **48**, 3033.
- M. Terrones, A. G. Souza Filho, and A. M. Rao, *Doped Carbon Nanotubes: Synthesis, Characterization and Applications* Vol. 111, 531–566 (Springer Topics in Appl. Phys., Springer, 2008).
- Rao, A. M., et al., *Nature* (1997) **388**, 257.
- Villapando-Paez F., et al., *Chem Phys Lett* (2006) **424**, 345.
- Subrahmanyam, K. S., et al., *J Phys Chem C* (2009) **113**, 4257.
- Das B., et al., *Chem Commun* (2008) **5**, 155.
- Panchakarla, L. S., et al., *Adv Mater* (2009) **21**, 4726.
- Dresselhaus, M. S. and Dresselhaus, G., *Adv Phys* (1981) **30**, 139.
- Ajayan, P. M., et al., *Nature* (1993) **362**, 522.
- Endo, M., et al., *J Appl Phys* (2001) **90**, 5670.
- Terrones, M., et al., *Full Sci Tech* **6**, 787 (1998).
- Goldberg, D., et al., *Carbon* (2005) **38**, 2017.
- Reddy, A. L. M., et al., *ACS Nano* (2010) **4**, 6337.
- Zhang C., et al., *Adv Mater* (2011) **23**, 1020.
- Costa, S. D., et al., *Carbon* (2011) **49**, 4719.
- Kalbac, M., et al., *Nano Lett* (2011) **11**, 1957.
- Shoushan, F., et al., *Nanotechnology* (2003) **14**, 1118.
- Rummeli, M. H., et al., *J Phys Chem C* (2007) **111**, 4094.
- Stuerzl, N., et al., *Phys Stat Sol B* (2009) **246**, 2465.
- Xiang, R., et al., *Jpn J Appl Phys* (2008) **47**, 1971.
- Simon, F., et al., *Phys Rev Lett* (2005) **95**, 017401.
- Simon, F., et al., *Phys Rev B* (2010) **81**, 125434.
- Miyauchi, Y., and Maruyama, S., *Phys Rev B* (2006) **74**, 035415.
- Malard, L. M., et al., *Phys Rep* (2009) **473**, 51.
- Castro Neto, A. H., et al., *Rev Mod Phys* (2009) **81**, 109.
- Jorio, A., Dresselhaus, M. S., Saito, R., and Dresselhaus, G. *Raman Spectroscopy in Graphene Related Systems*. WILEY-VCH, Weinheim, (2011).
- Novoselov, K. S., et al., *Nature* (2005) **438**, 197.
- Malard, L. M., et al., *Phys Rev Lett* (2008) **101**, 257401.
- Yan, J., et al., *Phys Rev Lett* (2008) **101**, 136804.
- Kotakoski, J., et al., *Phys Rev B* (2006) **74**, 245420.
- Lucchese, M. M., et al., *Carbon* (2010) **48**, 1592.
- Cancado, L. G., et al., *Nano Lett* (2011) **11**, 3190.
- Kotakoski, J., et al., *Phys Rev Lett* (2011) **106**, 105505.
- Meyer, J. C., et al., *Nat Mater* (2011) **10**, 209.
- Ma, J., et al., *Phys Rev B* (2009) **80**, 033407.
- Bhowmick, S., et al., *Phys Rev B* (2010) **81**, 155416.
- Banhart, F., et al., *ACS Nano* **5**, 26 (2011).
- Stone, A. J., and Wales, D. J., *Chem Phys Lett* (1986) **128**, 501.
- Li, L., et al., *Phys Rev B* (2005) **72**, 184109.
- Ma, J., et al., *Phys Rev B* (2009) **80**, 033407.
- Lee, G. D., et al., *Phys Rev Lett* (2005) **95**, 205501.
- El-Barbary, A. A., et al., *Phys Rev B* (2003) **68**, 144107.
- Jeong, B. W., et al., *Phys Rev B* **78**, 165403 (2008).
- Tsetseris, L., and Pantelides, S. T., *Carbon* (2009) **47**, 901.
- Lusk, M. T., and Car, L. D., *Phys Rev Lett* (2008) **100**, 175503.
- Jauregui, L. A., et al., *Sol Stat Comm* **151**, 1100 (2011).
- Kim, K., et al., *ACS Nano* (2011) **5**, 2142.
- Yu, Q., et al., *Nature Mat* (2011) **10**, 443.
- Ruiz-Vargas, C. S., et al., *Nano Lett* (2011) **11**, 2259.
- Jia, X., et al., *Science* (2009) **323**, 1701.
- Cançado, L. G., et al., *Phys Rev Lett* (2004) **93**, 047403.
- Cançado, L. G., et al., *Phys Rev Lett* (2004) **93**, 247401.
- Campos-Delgado, J., et al., *Nano Lett* (2008) **8**, 2773.
- Yang, L., et al., *Phys Rev Lett* (2007) **99**, 186801.
- Nakada, K., et al., *Phys Rev B* (1996) **54**, 17 954.
- Saito, R., et al., *Adv Phys* (2011) **60**, 413.
- Hashimoto, A., et al., *Nature* (2004) **430**, 870.
- Meyer, J. C., et al., *Nano Lett* (2008) **8**, 3582.
- Gass, M. H., et al., *Nature Nanotech* (2008) **3**, 676.
- Girit, C. O., et al., *Science* (2009) **323**, 1705.
- Warner, J. H., et al., *Nature Nanotech* (2009) **4**, 500.
- Wildoer, J. W. G., et al., *Nature* (1998) **391**, 59.
- Odom T. W., et al., *Nature* (1998) **391**, 62.
- Carroll, D. L., et al., *Phys Rev Lett* (1997) **78**, 2811.
- Maciel, I. O., et al., *Nature Mater* (2008) **7**, 878.
- Hartschuh, A., et al., *Phys Rev Lett* (2003) **90**, 095503.
- Qian H., et al., *Nano Lett* (2008) **8**, 2706.
- Georgi, C., and Hartschuh, A., *Appl Phys Lett*, (2010) **97**, 143117.
- Doorn, S. K., et al., *Phys Rev Lett* (2005) **94**, 016802.
- Elias, D. C., et al., *Science* (2009) **323**, 610.
- Robinson, J. T., et al., *Nano Lett* (2010) **10**, 3001.
- Cheng, S. H., et al., *Phys Rev B* (2010) **81**, 205435.
- Guo, B., et al., *Insciences J* (2011) **1**, 80.
- Hwang, E. H., et al., *Phys Rev B* (2007) **76**, 195421.
- Farmera, D. B., et al., *Appl Phys Lett* (2009) **94**, 213106.
- Biel, B., et al., *Phys Rev Lett* (2009) **102**, 096803.
- Hong, Woong-Ki., et al., *Nanotechnology* (2006) **17**, 5675.
- Skákalová, V., et al., *Phys Stat Sol B* (2008) **245**, 2280.
- Tuinstra, F., and Koenig, J. L., *J Phys Chem* (1970) **53**, 1126.
- Cancado, L. G., et al., *Appl Phys Lett* (2006) **88**, 163106.
- Lazzeri, M., and Mauri, F., *Phys Rev Lett* (2006) **97**, 266407.
- Beams, R., et al., *Nano Lett* (2011) **11**, 1177.
- Crespi, V. H., *Phys Rev B* (1996) **53**, 13303.
- Terrones, H., M. et al., *Phys Rev Lett* (2000) **84**, 1716.
- Huang, P. Y., et al., *Nature* (2011) **469**, 389.
- Lui, C. H., et al., *Nano Lett* (2011) **11**, 164.
- Cong C., et al., *ACS Nano* (2011) **5**, 8760.
- Lui, C. H., et al., *Nature Phys* (2011) **7**, 944.
- Das, A., et al., *Nature Nanotech* (2008) **3**, 210.
- Basko, D. M., et al., *Phys Rev B* (2009) **80**, 165413.
- Das, A., et al., *Phys Rev B* (2009) **79**, 155417.